Additive Manufacturing 36 (2020) 101719

Contents lists available at ScienceDirect

Additive Manufacturing

journal homepage: www.elsevier.com/locate/addma

Research Paper

Additively manufactured electrohydrodynamic ionic liquid pure-ion sources for nanosatellite propulsion

Dulce Viridiana Melo Máximo [a,b,1], Luis Fernando Velásquez-García [a,*,2]

[a] Microsystems Technology Laboratories, Massachusetts Institute of Technology, 77 Massachusetts Ave., Cambridge, MA 02139, USA
[b] Tecnologico de Monterrey, Escuela de Ingeniería y Ciencias, México City, México

ARTICLE INFO

Keywords:
3D-printed microelectromechanical system
EMI-BF_4
Ionic liquid ion source
Nanosatellite propulsion
Zinc oxide nanowire

ABSTRACT

This study reports the design, fabrication, and characterization of novel, low-cost, additively manufactured, miniaturized, multiplexed electrospray sources with zinc oxide nanowire (ZnONW)-based nanofluidics that produce, in both polarities, pure ions from ionic liquids. The devices comprise an emitting electrode with a monolithic array of emitters and an extractor electrode that triggers the electrohydrodynamic emission of ions from the emitter tips. The emitters are solid cones coated with a nanoporous, hydrothermally grown ZnONW forest that transports ionic liquid to the emitter tips. The emitting electrodes are 3D-printed using either SS 316L via binder jetting or FunToDo Industrial Blend resin via vat polymerization. The extractor electrode is 3D-printed using SS 316L via binder jetting. Experimental characterization of the devices in vacuum using an external collector electrode and the ionic liquid EMI-BF_4 shows bipolar pure-ion emission with maximum per-emitter current on the order of microamperes, maximum per-emitter thrust on the order of a fraction of a micronewton, and an average of ~95% beam transmission, resulting in 100% polydispersive efficiency and a significantly higher specific impulse for a given bias voltage compared to state-of-the-art devices. This development is of great interest for miniaturized spacecraft propulsion and focused ion beam applications.

1. Introduction

Spacecraft use rockets to maneuver in space, e.g., change the orbit, rendezvous with a station. Rockets produce thrust by ejecting a high-speed jet rearward, which, due to Newton's third law, causes a forward force on the engine [1]. An important metric of thruster efficiency is the specific impulse I_{sp}, defined as the thrust delivered per unit of weight flow rate. Currently, only chemical rockets are powerful enough to put a payload in space; however, the energy density of the chemical reactions harnessed by these rockets limits their I_{sp} to ~5×10^2 s [1]. Nonetheless, once a spacecraft is in space, alternative propulsive schemes can use the propellant more efficiently, albeit delivering significantly smaller force densities. In particular, engines commonly known as electrospray thrusters can electrohydrodynamically eject a high-speed stream of charged particles from a low-vapor pressure liquid propellant. Such engines are capable of bipolar operation, that is, they can emit either negatively or positively charged particles from the same propellant by simply changing the polarity of the extraction bias voltage [2].

The development of miniaturized spacecraft for performing target-focused missions using constellations that have associated reduced per-satellite and launching (shared rides) costs has attracted much research interest worldwide [3]. Nanosatellites are miniaturized satellites that weigh 1–10 kg (wet mass), typically corresponding to 1–12 U where 1 U is equal to 10 cm × 10 cm × 10 cm and less than 1.33 kg [4]. Multiple examples of scaled-down propulsion (micropropulsion) [5–7] and other nanosatellite subsystems made with precision machining and micro- and nanotechnology have been reported. Electrospray thrusters are an attractive choice for propelling nanosatellites because their physics favors miniaturization. For example, their start-up voltage scales with the square root of the emitter diameter. Also, their ability to emit both positively and negatively charged beams obviates the need of a neutralizer (i.e., an electron source that maintains the charge neutrality of the spacecraft) that could consume propellant at a rate comparable to that of miniaturized thrusters (e.g., hollow cathodes) or that could degrade in the presence of residual oxygen in low Earth orbit (LEO) (e.g.,

* Corresponding author.
E-mail address: Velasquez@alum.mit.edu (L.F. Velásquez-García).
[1] ORCID ID 0000-0001-7488-7677
[2] ORCID ID 0000-0002-9232-1244

https://doi.org/10.1016/j.addma.2020.101719
Received 2 September 2020; Received in revised form 9 November 2020; Accepted 12 November 2020
Available online 21 November 2020

thermionic cathodes, field-emission cathodes) [8].

Ionic liquids are salts that are liquid in standard environmental conditions. Ionic liquids are a good choice for electrospray propellant because they electrohydrodynamically eject solvated ions to produce high-I_{sp} thrust [9]. The ionic liquid 1-ethyl-3-methylimidazolium tetrafluoroborate (EMI-BF_4; molecular weights of its constitutive ions EMI^+ and $BF4^-$ are 111.2 Da and 86.8 Da, respectively [10]) is commonly used as an electrospray propellant owing to its high electrical conductivity (S/m level), negligible vapor pressure, and near-symmetric bipolar emission. Numerous miniaturized ionic liquid electrospray thrusters, including many that use EMI-BF_4 as the electrospray propellant, have been reported [11–19]. In these devices, miniaturization via microfabrication and precision machining reduces the bias voltage needed to operate the engine and facilitates the creation of monolithic, dense, uniform arrays of emitters that greatly increase the engine thrust compared to a single-emitter device. Ion emission is attained by feeding the propellant to each emitter using a large hydraulic impedance that restricts the emitter flow rate; examples of these micro-/nanofluidic structures include capillaries filled with microspheres (e.g. [13]), nanostructured porous films (e.g. [16]), and bulk-porous emitters (e.g. [14]). However, although capable, these devices are produced using subtractive manufacturing methods that are very expensive and time-consuming; in addition, the miniaturized thrusters emit other species besides pure ions, thereby impacting their propulsive efficiency and I_{sp}.

Additive manufacturing (AM) comprises the use of fabrication methods that join materials into solid objects, usually in a layer-by-layer manner [20]. Many mainstream AM techniques are also microfabrication processes as they create objects using volume elements (voxels) with dimensions of the order of micrometers or tens of micrometers. Consequently, AM has been recently explored to create a wide range of microelectromechanical systems (MEMS), particularly microfluidics [21–24] including multiplexed electrospray droplet sources [25,26]. This study reports the first proof-of-concept demonstration of low-cost, additively manufactured, MEMS multiplexed electrospray sources with zinc oxide nanowire (ZnONW) nanofluidics (i.e., a fluidic system with a sub-micron characteristic dimension that dominates the fluid dynamics [27]), including the first fully additively manufactured devices, that emit pure ions of both polarities from ionic liquids. The manufacture of such devices via 3D printing and hydrothermal growth could help democratize nanosatellite propulsion technology and shorten design iteration loops, as AM quickly and cheaply produces complex or customized devices in small- or medium-sized batches [28]. Thus, AM is a significant improvement over the time-consuming and expensive precision subtractive manufacturing and semiconductor cleanroom microfabrication methods employed for producing the previously reported devices. This study investigates two different designs: a design with an emitter array made of 3D-printed SS 316L (a corrosion-resistant, non-magnetic stainless steel) via binder jetting and a design with an emitter array made of FunToDo Industrial Blend resin (FTD-IB—a highly cross-linked, acrylic based polymer) via vat polymerization. This study aims to explore any trade-offs between device cost and device performance while using EMI-BF_4 as the working fluid.

2. Materials and methods

2.1. Device designs

The MEMS multiplexed electrospray devices are square diodes, composed of an emitting electrode and an extractor electrode (Fig. 1). These devices emit pure ions when fed with EMI-BF_4 and a high voltage is biased across the two electrodes. The emitting electrode includes a fluidic connector, a liquid reservoir, a monolithic array of externally fed emitters (i.e., solid, sharp cones coated with a conformal, dense, hydrothermally grown ZnONW forest), spill guards, and a wall that protects the emitter array. The ZnONWs greatly increase the wettability of the emitters with respect to EMI-BF_4 [29] (Fig. 2a–d), thereby creating a nanostructured material with open pores that transports the ionic liquid to the emitter tips [11,12,16]. The liquid reservoir has an array of columns that uniformly distributes the ionic liquid to feed it to an array of openings at its ceiling, which in turn supply ionic liquid to the bases of the emitters. The emitting electrodes are made of SS 316L (Figs. 1a and 3a) or FTD-IB resin (Figs. 1b and 3e). In both cases, the emitter height is below the maximum long-term raise of EMI-BF_4 on a vertical 3D-printed surface coated with a dense, conformal forest of ZnONWs (Fig. 2e). The extractor electrode is a plate made of SS 316L with an array of proximal apertures, arranged so that each aperture is concentric to the corresponding emitter axis when assembled. The fluidic connector is a threaded hole. The two kinds of emitting electrode designs (i.e., metal-based and polymer-based) differ in terms of the emitter height, emitter tip diameter, structural support of the emitter array, and capabilities of the printing methods employed. In particular, the dimensions used in the designs are based on the minimum features that can be manufactured, expected misalignment, and manufacturing precision. Furthermore, printing the FTD-IB emitter array with high precision requires full structural support, in the form of extraneous material underneath, surrounding the fluidic connector. In contrast, in SS 316L binder jetting printing, the powder bed provides the necessary structural support [20]).

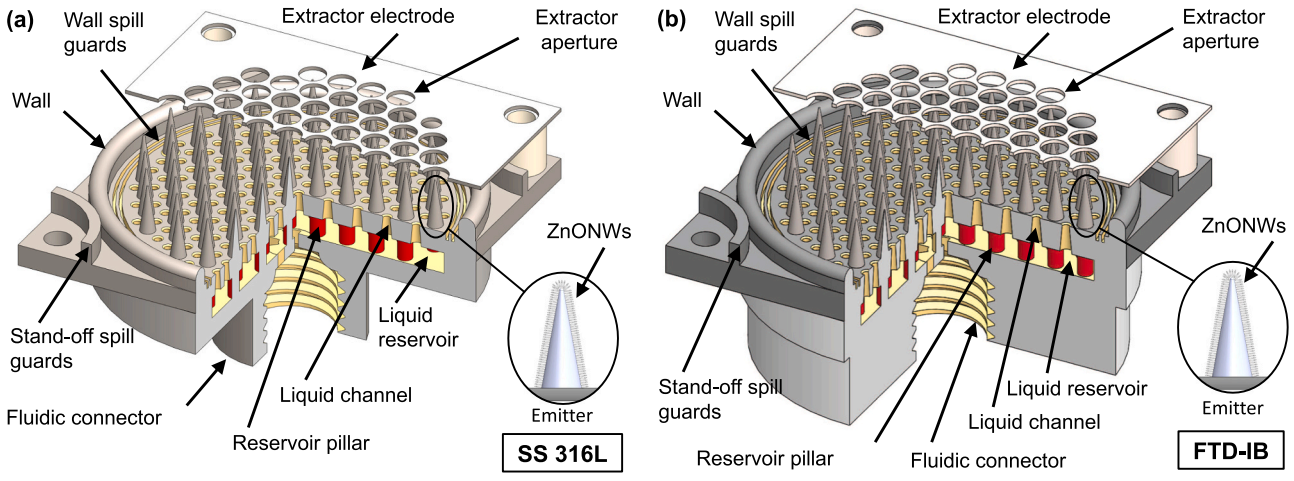

Fig. 1. 3D schematics of 3D-printed MEMS multiplexed electrospray ionic liquid ion sources. (a) 3D schematic of devices with emitting electrodes made of SS 316L. (b) 3D schematic of devices with emitting electrodes made of FTD-IB.

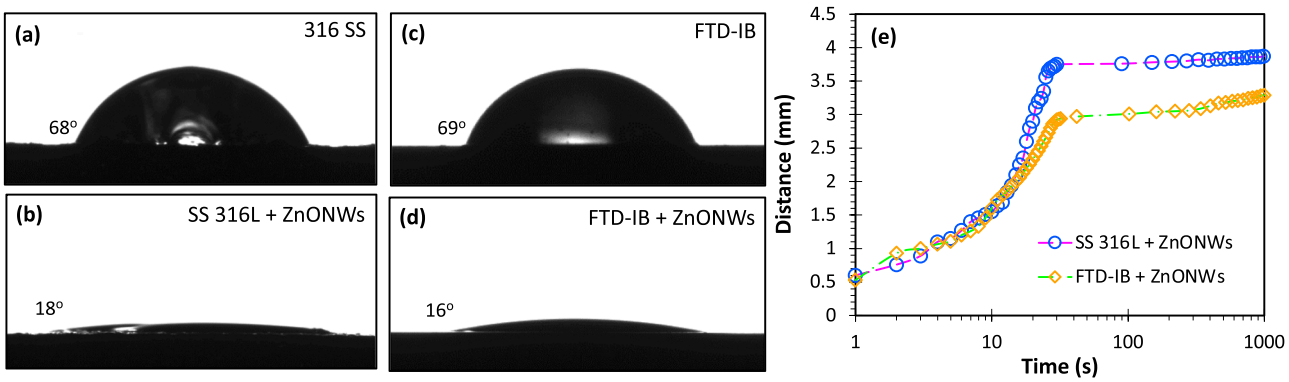

Fig. 2. Wettability of 3D-printed samples with and without ZnONWs using EMI-BF_4 as working liquid. Wetting angle of EMI-BF_4 on (a) 3D-printed SS 316L, (b) 3D-printed SS 316L covered with a ZnONW forest, (c) 3D-printed FTD-IB, and (d) 3D-printed FTD-IB covered with a ZnONW forest. Each reported contact angle is the average of 40 measurements on flat samples uncoated and coated with thermally grown ZnONWs using 10 μL EMI-BF_4 droplets with a Ramé-hart goniometer and the DROP image software. (e) Height of EMI-BF_4 wetting front versus time on a vertical, flat wall made of 3D-printed SS 316L covered with a ZnONW forest, and on a vertical, flat wall made of FTD-IB covered with a ZnONW forest.

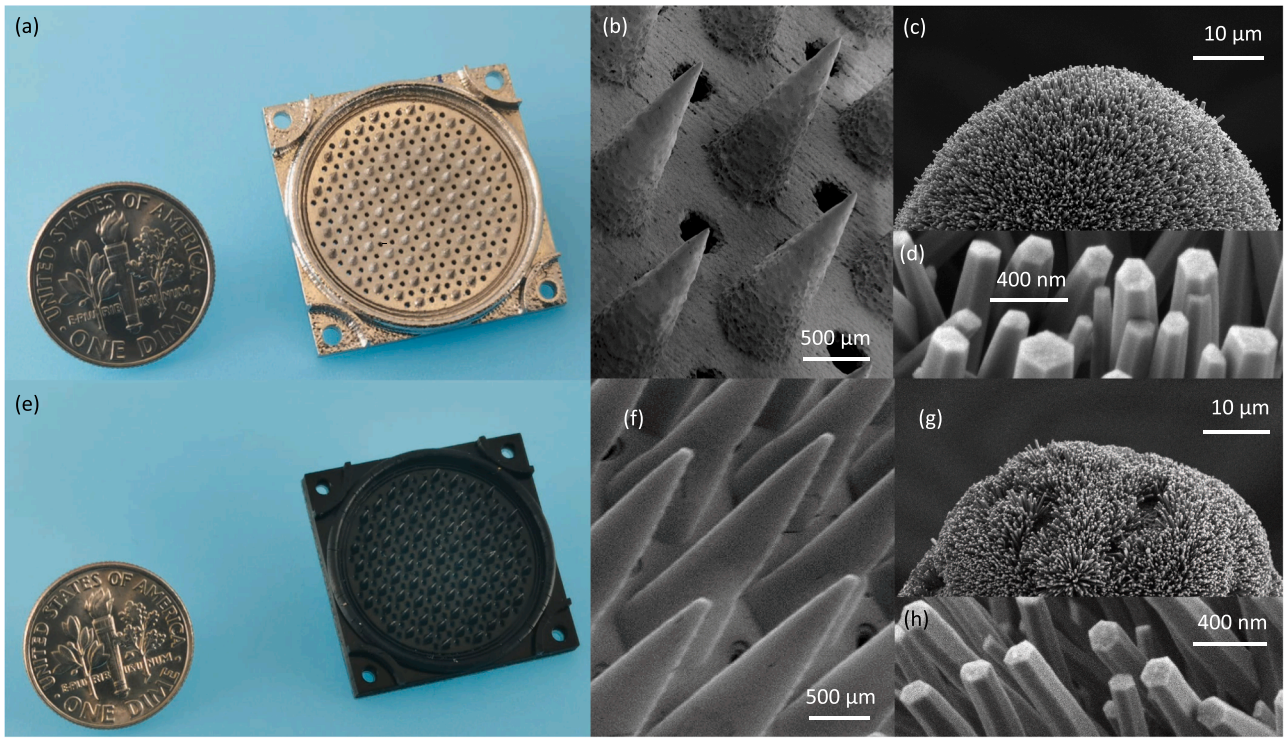

Fig. 3. Optical images of fabricated emitting electrodes. (a) Optical image of 3D-printed emitting electrode made of SS 316L next to a US dime, (b) close-up SEM image of its emitter array, (c) close-up SEM image of an emitter tip conformally coated with a dense ZnONW forest, and (d) close-up SEM image of the ZnONW forest. (e) Optical image of 3D-printed emitting electrode made of FTD-IB next to a US dime, (f) close-up SEM image of its emitter array, (g) close-up SEM image of an emitter tip conformally coated with a dense ZnONW forest, and (h) close-up SEM image of the ZnONW forest.

2.2. Device fabrication

A thorough description of the fabrication of the devices is included in a separate electronic supplementary information (ESI) document. The devices are 3D-printed using SS 316L via binder jetting by i.materialise (Leuven, Belgium) and using FTD-IB resin (Fun To Do, Alkmaar, The Netherlands) via vat polymerization with a digital light projection (DLP) 3D printer Asiga MAX X27 UV (Asiga, Alexandria, Australia). The ZnONWs are hydrothermally grown using a home-built reactor. The constitutive materials were down-selected after characterizing a wide variety of 3D printable feedstock on aspects such as printing resolution, chemical compatibility with EMI-BF_4 and with the ZnONW hydrothermal growth process, and capability to grow dense ZnONW forests on the surface of printed objects [30]. Furthermore, binder-jetting-printed SS 316L has been shown to be ultra-high vacuum (UHV) compatible [31] and has been used in miniaturized, multiplexed high-electric field devices such as corona gas pumps [32]. Likewise, photopolymerizable acrylate-based resins similar to FTD-IB have been shown to outgas at the level of vacuum-compatible elastomers [33].

After being printed, the tips of the metal emitting electrodes are sharpened using a home-built electrochemical cell comprised of a beaker containing a chemical mix, a sample holder (anode), a counter-electrode (cathode), and a glass plate. The sample to be polished is first ultrasonically cleaned for 5 min in an isopropanol bath and dried with nitrogen. Next, the sample is mounted on the sample holder, with the emitters positioned face-down. Then, the holder is connected to the

positive terminal of a RIGOL DP832A direct-current power supply (Rigol Technologies, Beaverton, OR, USA) and the counter-electrode (a 0.61-mm-thick SS 316L sheet) is connected to the negative terminal of the power supply. The glass plate is then attached to the wall of the beaker with Kapton tape, thereby restricting the electrolyte's line of sight to the counter-electrode to help uniformly and isotropically etch the sample. The beaker is then filled with the electrolyte (H_3PO_4:H_2SO_4:H_2O volume mix of 13.5:9:7.5 [34]) at room temperature. The amount of metal removed depends on the specific bath, temperature, current density, and the particular metallic workpiece being electropolished. In practice, the amount of metal removed is varied by controlling the magnitude of the current fed to the electrochemical cell and its duration [35]; typical etch jobs take tens of minutes and involve A-level currents, while the sample is rotated every 5 min to improve etch uniformity.

ZnONWs are hydrothermally grown on top of both kinds of emitters (i.e., metal-based and polymer-based) at 90 °C by using a 1:1 by volume solution of 0.025 M $Zn(NO_3)_2{\cdot}6H_2O$ in deionized water and 0.025 M hexamethylenetetramine in deionized water [36]. The ZnONWs grow on top of a 20-nm-thick ZnO seed layer previously deposited with an ATC Orion RF sputtering system (AJA International, Scituate, MA, USA); the seed layer is deposited using a shadow mask so that only the array of emitters and the inter-emitter surface are coated with the ZnO seed.

2.3. Device characterization

2.3.1. Current-voltage (I-V) characteristics

The *I-V* characteristics from 37-, 61-, and 85-emitter devices were collected, for both polarities, at 1×10^{-6} Torr using an external collector electrode separated 8.5 mm from their extractor electrode. For each test, 30 μL of EMI-BF_4 was supplied to the area coated with ZnONWs; the ZnONWs readily spread the liquid, coating all the emitters. The bias voltages on each of the three electrodes (emitting, extractor, and collector electrodes) were supplied using BERTAN 225 power supplies (Spellman, Hauppauge, NY, USA) that are capable of biasing up to 10 kV. In all experiments, the emitting electrode was grounded. The extractor voltage was swept with both polarities between 0 V and 7 kV in 50-V steps for devices with an FTD-IB emitting electrode and between 0 V and 4.25 kV in 50-V steps for devices with an SS 316L emitting electrode; it was unfeasible to apply larger bias voltages to the devices with an SS 316L emitting electrode due to the resultant unsteady operation. The collector was biased at 8 kV (FTD-IB emitting electrode) or at 6 kV (SS 316L emitting electrode), at the same polarity of the extractor voltage in order to collect the emitted beam. From the I-V data, the transmission efficiency n_{tr} (ratio of collected current to emitted current) can be estimated. The startup voltage V_{start} of the devices is given by [37]

$$V_{start} = \sqrt{\frac{\gamma R}{\varepsilon_o}} \ln\left(\frac{2G}{R}\right), \tag{1}$$

where γ is the surface tension of the liquid (4.52×10^{-2} N/m for EMI-BF_4), R is the tip radius, ε_o is the permittivity of free-space (8.854×10^{-12} F/m), G is the emitter tip-to-electrode separation (887 μm for FTD-IB devices and 862 μm for the SS 316L devices), and $2G \gg R$. The per-emitter I-V characteristics were estimated by dividing the total current by the number of emitters of the device.

2.3.2. Mass spectrometry of emitted plume

Mass spectrometry of the electrospray produced by 85-emitter devices operated at both polarities was conducted at 10^{-6} Torr using a commercial quadrupole mass spectrometer (Ardara Technologies, Ardara, PA, USA) capable of measuring mass spectra between 15 Da and 10 kDa in 0.1 Da increments. The mass spectrometer has a maximum resolution of 10,000:1.

2.3.3. Thrust and I_{sp} estimates

The thrust T produced by an electrospray thruster can be estimated from the *I-V*, mass spectrometry, and beam divergence data. The thrust is given by [12]

$$T = I_{coll}\sqrt{2V\langle m/q\rangle n_i n_\theta n_E n_p}\,, \tag{2}$$

where I_{coll} is the collector current, V is the extraction bias voltage, $\langle m/q\rangle$ is the average mass-to-charge ratio (from mass spectrometry data), n_i is the ionization efficiency (~1 for electrospray of EMI-BF_4 in the ionic regime [38]), and n_θ is the angular efficiency given by [38]

$$n_\theta = \frac{9}{\theta_o^6}(\sin\theta_o - \theta_o\cos\theta_o)^2, \tag{3}$$

where θ_o is the beam semi-angle, n_E is the energy efficiency (~98% for EMI-BF_4 electrospray in the ionic regime [38]), and n_p is the polydispersive efficiency (a measure of how much less thrust is produced by a beam composed of particles with different speeds compared to a beam where all particles have the same speed). The specific impulse is given by

$$I_{sp} = \frac{T}{I\langle m/q\rangle g}, \tag{4}$$

where I is the emitted current and g is the gravitational constant.

3. Results

3.1. Fabrication results

Table 1 summarizes the metrology of resolution matrices (arrays of straight, circular cylinders with varying diameter and height) made of the two printable materials employed in this study. The metrology was conducted with a VK-X 3D confocal laser microscope (Keyence Corporation of America, Itasca IL, USA). Excellent linearity is seen between the printed features and the computer-aided design (CAD) features for both materials. Although the scaling factors of 3D-printed SS 316L are closer to unity, they are repeatable for both materials and can be compensated for at the CAD design stage. The in-layer and out-of-layer offsets of 3D-printed FTD-IB are significantly smaller, and the material can also resolve smaller features; however, the metal parts can be uniformly electrochemically polished to attain smaller dimensions than those achievable using FTD-IB. The dimensions of the fluidic connector were iterated using a resolution matrix spanning internal diameters between 5.5 and 7.0 mm in 0.1-mm steps; CAD inner diameters of 6.1 mm and 6.0 mm correspond to working 1/4"-28 threaded connectors made of SS 316L and of FTD-IB, respectively.

The fabricated devices are square diodes with side equal to 25.4 mm

Table 1
Summary of metrology of resolution matrices made of SS 316L via binder jetting and made of FTD-IB via vat polymerization.

Material	In-layer linearity	In-layer offset (μm)	In-layer MFS[c] (μm)	Out-of-layer linearity	Out-of-layer offset (μm)
SS 316L	PD[a] = 1.04·CD[b], R^2 = 0.999	129.4	285	PH[d] = 0.97·CH[e], R^2 = 0.999	106.9
FTD-IB	PD = 1.08·CD, R^2 = 0.986	11.6	64	PH = 0.92·CH, R^2 = 0.997	2.0

[a] Printed diameter.
[b] CAD diameter.
[c] Minimum feature size.
[d] Printed height.
[e] CAD height.

and height equal to 10.0 mm (i.e., 6.45 cm^3 enclosing volume). The devices have 37, 61, or 85 emitters with hexagonal packing in a 2-cm-diameter active area (2.7×10^1 emitters/cm^2). The metal emitters (Fig. 3a) have a height and tip diameter equal to 2.2953 mm ± 39.5 μm and 56.2 μm ± 3.7 μm, respectively; these dimensions result from uniformly sharpening the emitters via electropolishing from as-printed 307.45 μm ± 7.32 μm tip diameter (i.e. over a fivefold reduction) and as-printed 2.4790 mm ± 14.54 μm emitter height. The polymeric emitters have a height and tip diameter equal to 3.1530 mm ± 32.0 μm and 107.4 μm ± 15.4 μm, respectively. In both cases (i.e., metal emitting electrode and polymeric emitting electrode), the liquid reservoir has an array of 200-μm-diameter openings at its top to supply ionic liquid to the emitters. The extractor electrode is a 0.25 mm-thick SS 316L plate with an array of 1.8-mm-diameter proximal apertures aligned to the emitter array. A metal emitting electrode weighs 20.6 g (dry), while a polymeric emitting electrode weighs 4.3 g (dry), and an extractor electrode weighs 0.7 g.

The metrology of ZnONW forests on top of 3D-printed emitters was conducted with a Carl Zeiss 1525 field emission scanning electron microscope (Carl Zeiss AG, Oberkochen, Germany). The ZnONWs grown on top of 3D-printed SS316L emitters have diameters in the 45–345 nm range (Fig. 4a) and separations in the 91–770 nm range (Fig. 4b), resulting in an average NW diameter equal to 141 nm ± 53 nm and an average NW separation equal to 236 nm ± 129 nm. Similarly, the ZnONW forests grown on top of 3D-printed FTD-IB emitters have diameters in the 95–275 nm range (Fig. 4c) and separations in the 61–362 nm range (Fig. 4d), resulting in an average NW diameter equal to 173 nm ± 32 nm and an average NW separation equal to 164 nm ± 57 nm. X-ray diffraction (XRD) studies of flat 3D-printed samples covered with hydrothermally grown ZnONWs were performed using a Bruker D8 General Area Detector Diffraction System (GADDS) diffractometer (Bruker Corporation, Billerica, MA, USA) with a cobalt source (λ = 1.790 Å). The XRD pattern of the 3D-printed SS 316L sample coated with ZnONWs consists of the substrate signal (austenitic matrix, i.e., γ-Fe, ICDD File Card 33–0397) and all of the ZnO peaks from a hexagonal wurtzite structure [39] (ICDD file chart 36–1451), implying that pure ZnO was synthesized (Fig. 4e). Moreover, the high (002) peak at 40° indicates that the nanowires are highly c-oriented, as also confirmed through SEMs (Fig. 3c and d). The XRD pattern of the 3D-printed FTD-IB sample coated with ZnONWs indicates the amorphous nature of the resin substrate, and the high (002) peak indicates that the ZnO structure of the coating with c-axis nanowires was oriented normal to the substrate (Fig. 4e), as also confirmed through SEM (Fig. 3g and h).

3.2. I-V characteristics

The per-emitter collected current and transmission efficiency versus extractor bias voltage for the devices with an SS 316L emitting electrode are shown in Fig. 5a and b, respectively. In these devices, the per-emitter *I-V* characteristics are similar and approximately symmetric, although the negative emission is on average 24% larger; the average maximum per-emitter collected current with positive and negative polarity is 1.72 μA and 2.13 μA, respectively. The average transmission efficiency is 95.9%. The average experimental start-up voltage is 9% larger than the estimate from Eq. 1(1.56 kV).

Similarly, the per-emitter collected current and transmission efficiency versus extractor bias voltage for the devices with an FTD-IB emitting electrode are shown in Fig. 5c and d, respectively. In these devices, the per-emitter *I-V* characteristics are also similar and approximately symmetric, with the negative emission being 20% larger on average; the average maximum per-emitter collected current with

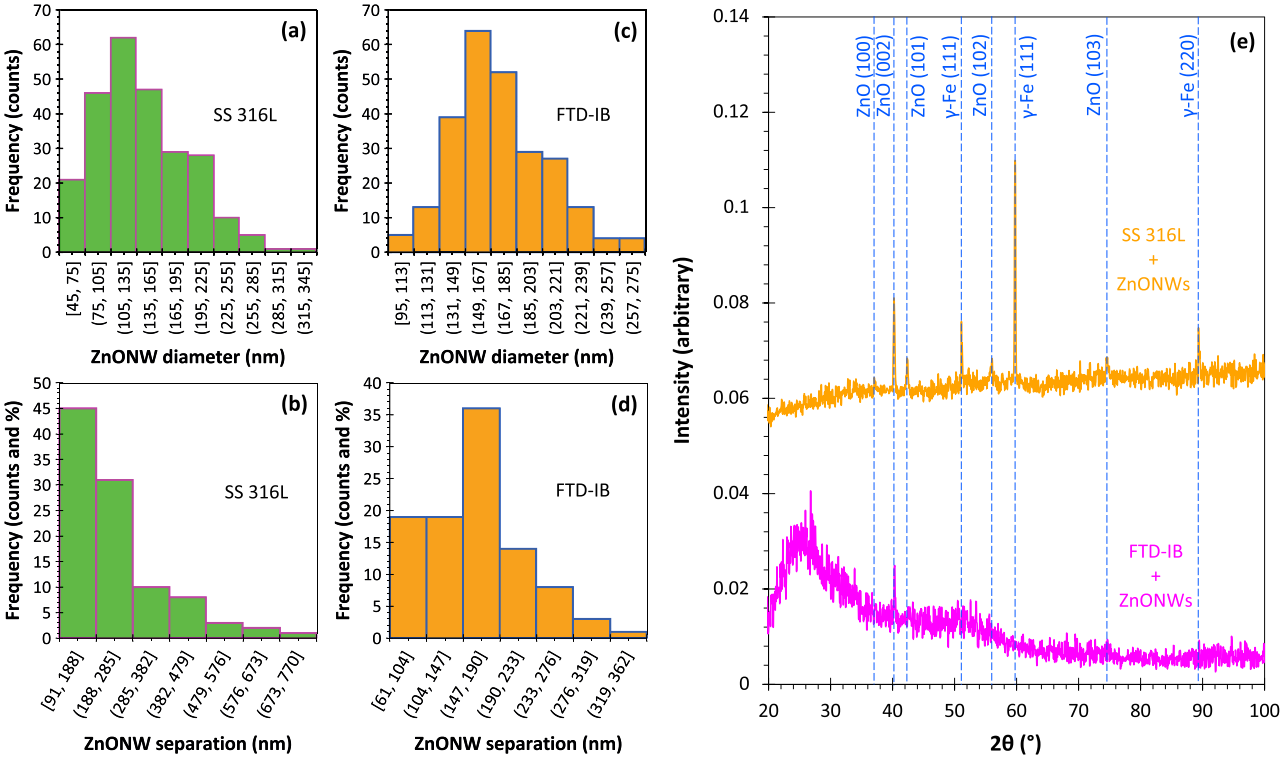

Fig. 4. Histograms of NW diameter and separation in hydrothermally grown ZnONW forests on top of 3D-printed substrates. (a) Histogram of the NW diameter in ZnONW forests hydrothermally grown on top of 3D-printed SS 316L. (b) Histogram of the NW separation in ZnONW forests hydrothermally grown on top of 3D-printed SS 316L. (c) Histogram of the NW diameter in ZnONW forests hydrothermally grown on top of 3D-printed FTD-IB. (d) Histogram of the NW separation in ZnONW forests hydrothermally grown on top of 3D-printed FTD-IB. (e) XRD patterns of a 3D-printed SS 316L sample coated with hydrothermally grown ZnONWs and of a 3D-printed FTD-IB sample coated with hydrothermally grown ZnONWs.

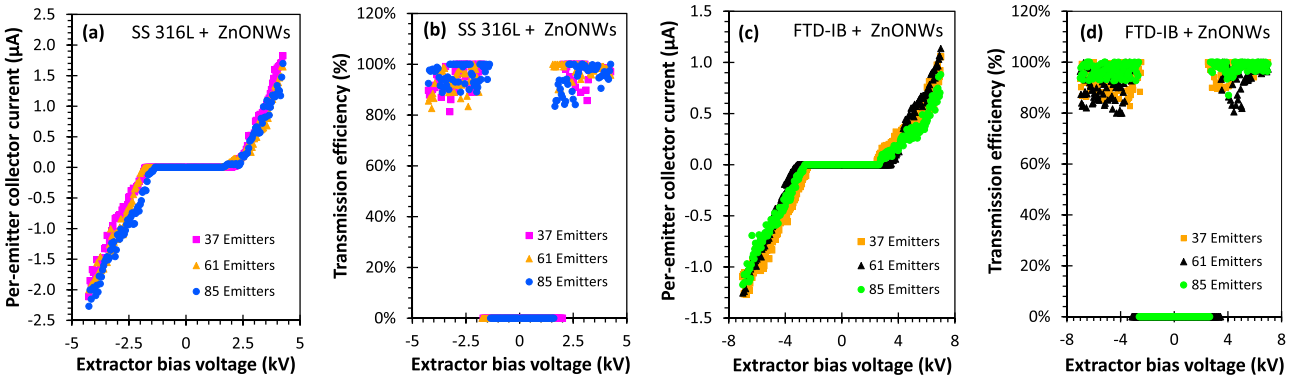

Fig. 5. *I-V* characteristics. (a) Per-emitter collected current versus extractor bias voltage and (b) transmission efficiency versus extractor bias voltage for devices with SS 316L emitting electrode. (c) Per-emitter collected current versus extractor bias voltage and (d) transmission efficiency versus extractor bias voltage for devices with FTD-IB emitting electrode.

positive and negative polarity is 1.02 μA and 1.23 μA, respectively. However, the maximum per-emitter collector currents are almost half of those of the SS 316L devices. The average transmission efficiency is 95.2%, which is similar to that of the SS 316L devices. The average experimental start-up voltage is 50% larger than the estimate from Eq. (1), that is, 1.832 kV, and two-thirds larger than the start-up bias voltage of SS 316L devices. Overall, the results indicate that the devices with an FTD-IB emitting electrode produce significantly lower per-emitter current for a given extractor bias voltage compared to the devices with an SS 316L emitting electrode.

3.3. Mass spectra of plume

Fig. 6 shows the mass spectra of the emitted plume with both polarities for devices with SS 316L (Fig. 6a) and FTD-IB (Fig. 6b) emitting electrodes. In both cases, for positive polarity, the only peak observed corresponds to EMI^+, and no peaks for the dimer, trimer, or larger species are observed. Similarly, in both cases, for negative polarity, the only peak corresponds to $BF4^-$; no peaks of larger species are observed. The mass spectra from the FTD-IB devices have a larger noise floor compared to those from the SS 316L devices, and the ratio between the positive and the negative peaks is significantly larger (2.26 vs. 1.42); nonetheless, the ratios of the different peaks of the mass spectra is known to significantly vary between tests [38]. Larger mass range scans did not reveal further peaks, specially the broad peak centered around 6.258 kDa associated with droplet emission that other researchers have reported for electrospray emitters using EMI-BF_4 [40], and an inspection of the collector electrode after the tests did not show evidence of droplets emitted. We speculate that the production of only ions is related to the ZnONWs. For example, reported electrospray devices fed with EMI-BF_4 that use nanofluidics made of black silicon (a grass-like nanostructured silicon surface created via plasma etching) emit pure ions, ions plus an EMI-BF_4 molecule, and ions plus two EMI-BF_4 molecules [12], and electrospray devices fed with EMI-BF_4 that use nanofluidics made of plasma-enhanced chemical vapor deposited (PECVD) carbon nanotube (CNT) forests emit pure ions and ions plus an EMI-BF_4 molecule [16]. Moreover, reported electrospray devices made of ceramic and fed with EMI-BF_4 can only operate in the negative polarity as they trigger a corona discharge when operated in the positive polarity [19].

Emitting only one species with each polarity implies that the polydispersive efficiency is 100%. The pure ionic emission with both polarities for both designs is significant because, to the best of our knowledge, all the literature on miniaturized ionic liquid electrospray sources have reported mass spectra with pure ions plus other species (e.g., ion coalesced with a EMI-BF_4 molecule, ion coalesced with two EMI-BF_4 molecules, droplets) [11–19].

3.4. Plume divergence

The device operation can be verified visually as it produces a faint

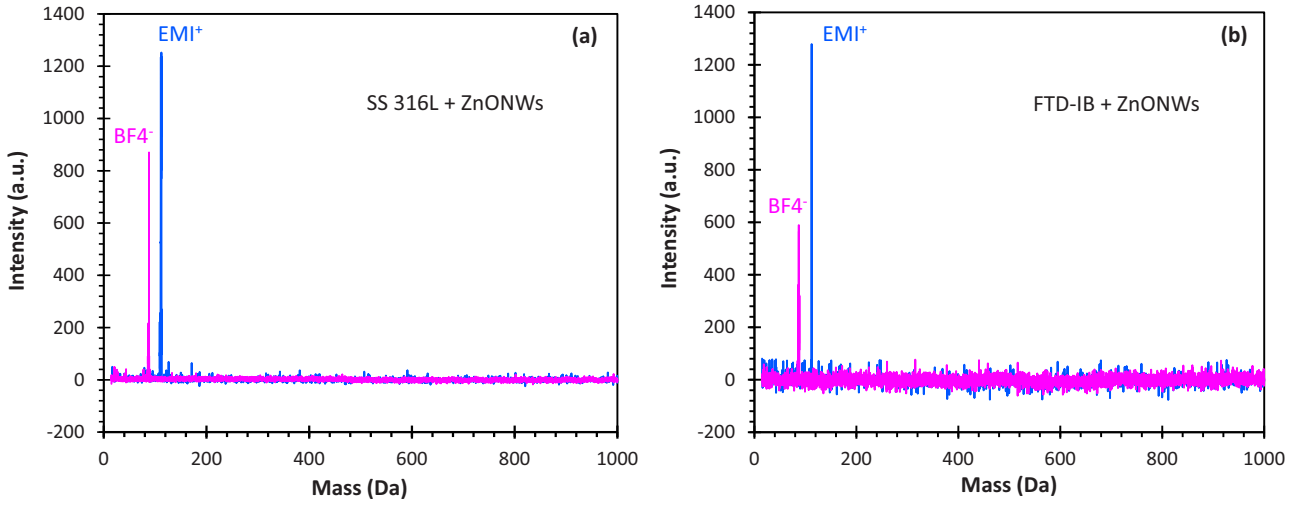

Fig. 6. Mass spectra of the emitted plume with positive and negative polarities. (a) Mass spectra of devices with 3D-printed SS 316L electrospray emitters coated with thermally grown ZnONWs. (b) Mass spectra of devices with 3D-printed FTD-IB electrospray emitters coated with thermally grown ZnONWs.

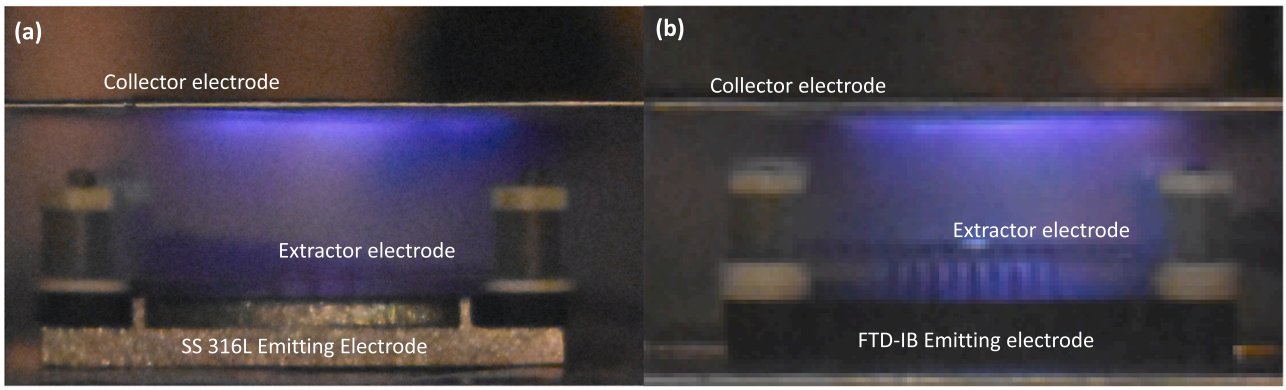

Fig. 7. MEMS multiplexed electrospray ionic liquid ion sources in operation. (a) Device with 3D-printed SS 316L electrospray emitters coated with thermally grown ZnONWs in operation. (b) Device with 3D-printed FTD-IB electrospray emitters coated with thermally grown ZnONWs in operation.

bluish glow between the extractor electrode and the collector electrode (Fig. 7). The same glow has been reported in Si MEMS multiplexed ionic liquid ion sources with black silicon nanofluidics [41]. In general, all tips in the array were lit, and the brightness across the beam was relatively uniform. The beam divergence was estimated by looking at the imprint of the glow on the collector electrode, resulting in an average beam semiangle of 30° and 25° for devices with SS 316L and FTD-IB emitters, respectively; these values are similar to those reported for a wide variety of miniaturized ionic liquid electrospray devices [11–19]. By using Eq. (3), the angular efficiency of devices with metal and polymeric emitters is estimated to be 94.6% and 96.3%, respectively.

3.5. Thrust and I_{sp} estimates

The per-emitter thrust (Eq. (2)) and specific impulse (Eq. (4)) versus the extractor bias voltage for devices with an SS 316L emitting electrode are shown in Fig. 8a and b, respectively, and those for devices with an FTD-IB emitting electrode are shown in Fig. 8c and d, respectively. In Fig. 8a and c, the per-emitter thrust vs extractor voltage is approximately symmetric and similar for both SS 316L and FTD-IB devices. The maximum per-emitter thrust is estimated to be 191.3 nN and 139.9 nN for SS 316L emitters and FTD-IB emitters, respectively. These values are similar; however, devices with an SS 316L emitting electrode produce significantly more thrust at the same extractor bias voltage. The maximum specific impulse is estimated to be 9.26×10^3 s and 1.22×10^4 s for devices with an SS 316L emitting electrode and FTD-IB emitting electrode, respectively. Given that the two types of devices produce pure ions with both polarities, the larger specific impulse attained by the polymeric devices is due to the larger bias voltage that is required to operate such devices.

4. Discussion

The *I-V* data (Section 3.2) suggest that devices with an SS 316L emitting electrode show better overall performance than devices with an FTD-IB emitting electrode. This is because devices with an SS 316L emitting electrode have sharper tips that turn-on at a lower bias voltage and have shorter emitters that, combined with their better spreading of EMI-BF_4 across the ZnONW forest (e.g., Fig. 2e), results in larger emitted currents at a given extractor bias voltage. The metal devices produce considerably higher thrust at the same extractor bias voltage, and metal-based devices are expected to last longer in space than polymeric-based ones. However, polymeric devices can be made using much cheaper printing hardware (as of October 2020, a typical binder jetting metal 3D printer costs around US $1M whereas a top-of-the line desktop vat polymerization 3D printer costs ~US $15,000), making polymer AM technology more readily available to more investigators and entrepreneurs. Consequently, devices with an FTD-IB emitting electrode could play an important role in truly inexpensive nanosatellite hardware, such as college-led, highly focused space missions.

Table 2 summarizes the reported literature on miniaturized, multiplexed ionic liquid electrospray sources with a comparable or greater number of emitters than in the devices reported in this study. This study has the lowest emitter density; this is understandable as the devices studied reflect the current capabilities of printing systems (~30 μm voxels). Improvements in 3D printing hardware are expected to bridge this gap. For example, DLP vat polymerization printers are based on Texas Instrument's DMD chip, of which there is currently a version with

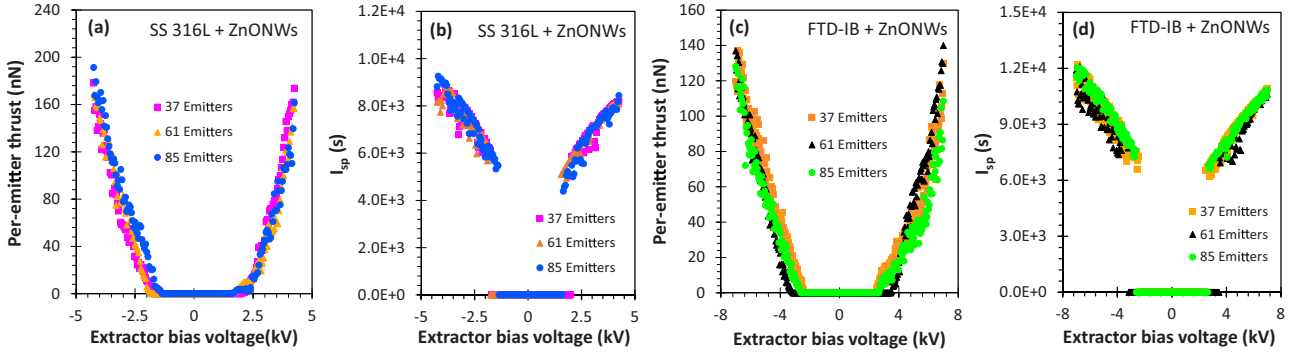

Fig. 8. Per emitter thrust and specific impulse from additively manufactured electrospray thrusters estimated using *I-V*, mass spectrometry, and plume divergence data. (a) Estimated per-emitter thrust versus extractor bias voltage and (b) estimated specific impulse versus extractor vias voltage for devices with 3D-printed SS 316L electrospray emitters coated with thermally grown ZnONWs. (c) Estimated per-emitter thrust versus extractor bias voltage and (d) estimated specific impulse versus extractor vias voltage for devices with 3D-printed FTD-IB electrospray emitters coated with thermally grown ZnONWs.

Table 2
Constitutive material, manufacturing method, working liquid, emitter density, number of emitters, maximum current per emitter, maximum thrust per emitter, maximum I_{sp}, maximum voltage, bipolar emission, and emitted species in representative studies of miniaturized, multiplexed, ionic liquid electrospray sources.

Ref.	Material	Manufacturing method	Working liquid	Emitter density (emitters/cm^2)	Number of Emitters	Max. current per emitter (μA)	Max. thrust per emitter (nN)	Max. I_{sp} (s)	Max. voltage (kV)	Tested bipolar? (Y/N)	Emitted species
[13]	Silicon	Microfabrication	EMI-Im	1.80×10^3	19	0.021	2	4.6×10^3	1.20	Y	EMI^+, (EMI-Im) EMI^+, droplets
[42]	Silicon	Microfabrication	EMI-BF_4	1.54×10^3	19	0.084	15	5.2×10^2	1.00	N	EMI^+, (EMI-BF_4) EMI^+, droplets
[15]	Silicon	Microfabrication	EMI-BF_4	2.13×10^2	127	0.25	16.5	4.7×10^2	0.85	Y	EMI^+, (EMI-BF_4) EMI^+, BF_4^-,(EMI-BF_4) BF_4^-, droplets
[18]	Borosilicate	Micromachining, laser ablation	EMI-BF_4	4.80×10^2	480	0.31	26	1.2×10^3	0.90	Y	Ion clusters, droplets
[6]	Borosilicate	Micromachining, laser ablation	EMI-BF_4	4.80×10^2	480	0.31	29	7.4×10^2	0.97	Y	EMI^+, (EMI-BF_4) EMI^+, BF_4^-,(EMI-BF_4) BF_4^-, droplets
[43]	Silicon	Microfabrication	EMI-BF_4	4.44×10^2	502	0.5	25	3.0×10^3	1.20	Y	EMI^+, (EMI-BF_4) EMI^+, (EMI-BF_4)$_2$ EMI^+, BF_4^-, (EMI-BF_4) BF_4^-,(EMI-BF_4)$_2$ BF_4^-, droplets
[16] (cones)	Silicon + CNTs	Microfabrication	EMI-BF_4	8.1×10^1	81	8	410	4.3×10^3	1.80	Y	EMI^+, (EMI-BF_4) EMI^+, BF_4^-, (EMI-BF_4) BF_4^-, droplets
[16] (pencils)	Silicon + CNTs	Microfabrication	EMI-BF_4	1.9×10^3	1900	0.7	39	3.7×10^3	1.20	Y	EMI^+, (EMI-BF_4) EMI^+, BF_4^-,(EMI-BF_4) BF_4^-
[11]	Silicon+ black silicon	Microfabrication	EMI-BF_4	1.60×10^3	1024	3	27	4.9×10^3	2.15	Y	EMI^+, (EMI-BF_4) EMI^+, BF_4^-, (EMI-BF_4) BF_4^-, droplets
[44]	Silicon	Microfabrication	EMI-Im	1.00×10^2	64	0.13	120	2.4×10^2	1.76	N	Ions, droplets
This study	SS 316L	Binder jetting	EMI-BF_4	2.7×10^1	37	2.11	180	8.7×10^3	4.25	Y	EMI^+, BF_4^-
					61	2	170	8.9×10^3	4.25		
					85	2.27	193	9.3×10^3	4.25		
This study	FTD-IB	Vat polymerization	EMI-BF_4	2.7×10^1	37	1.27	140	1.2×10^4	7.00	Y	EMI^+, BF_4^-
					61	1.25	140	1.2×10^4	7.00		
					85	1.18	130	1.2×10^4	7.00		

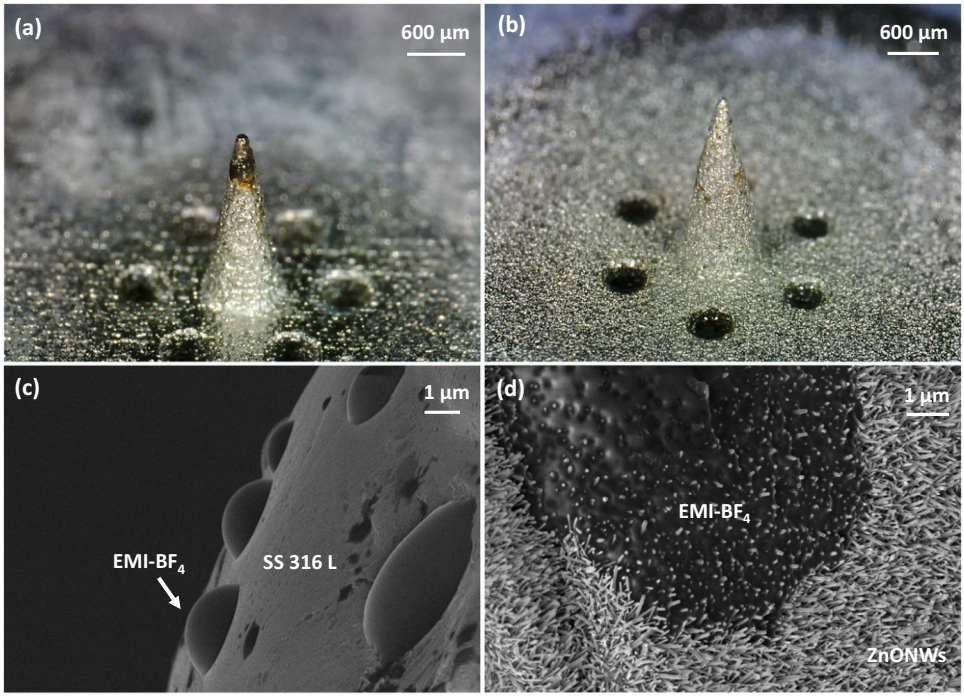

Fig. 9. Preliminary experimental results suggesting the reported devices have a long life. (a) Optical image of an SS 316L emitter after been operated in DC for several hours—the emitter is coated with a thin electrochemical crust. (b) Optical image of an SS 316L emitter after been cleaned by flushing DI water. (c) Close-up SEM of an electropolished SS 316L emitter without ZnONWs —the material is hydrophobic to the ionic liquid EMI-BF_4. (d) Close-up SEM of an electropolished SS 316L emitter coated with a forest of ZnONWs —the ZNONWs make the surface hydrophilic to EMI-BF_4, spreading well the ionic liquid.

a 5.4-µm pixel pitch [45]. If such a chip is used in a DLP 3D printer, it would result in a roughly thirtyfold increase in density of tips that are an order of magnitude sharper compared to those of the polymeric devices reported in this study. The maximum per-emitter currents and per-emitter thrusts are among the highest reported; however, for the latter parameter, it should be noted that this study uses bias voltages that are significantly larger than those used in other studies, resulting in higher thrust for the same current. In diode devices (i.e., those comprising an emitting electrode and an extractor electrode), the bias voltage used to extract current is the same bias voltage that sets the exit velocity of the stream of charged particles; however, in triode devices (i.e., those comprising an emitting electrode, an extractor electrode, and an accelerator electrode), the bias voltage for extraction is decoupled from the bias voltage used to set the exit speed [15]. Therefore, in principle, any of the devices listed in Table 2 could use a larger bias voltage than what was reported while still emitting a steady charged beam by integrating an accelerator electrode into the device. A more significant difference between the present study and previous ones is the I_{sp}; the I_{sp} from the 3D-printed devices is by far the highest value reported, due to the larger bias voltage used and, more importantly, owing to the 100% polydispersity efficiency that results in a smaller average mass-to-charge ratio of the plume. Studies of other miniaturized ionic liquid electrospray thrusters have reported the emission of ions plus other charged particles, such as an ion coalesced with one EMI-BF_4 molecule; the relative signal strength of this species is smaller than that of pure ions but still significant (30–50% of the ion peak [38]). Given the large mass difference between the pure ion and the ion plus an EMI-BF_4 molecule, the average mass-to-charge ratio is significantly larger, thereby affecting the I_{sp}.

The transmission efficiency of the extractor electrode is on par with that of microfabricated devices (e.g., [12]). However, care must be taken when assembling the 3D-printed devices to ensure that the emitter tips are concentric to the extractor apertures by, for example, examining the assembly under magnification. This condition would relax by printing more precisely the devices using smaller voxels and/or by integrating active, compliant structures that provide a robust assembly that can compensate for perturbations [46,47].

This study reports the first proof-of-concept demonstration of low-cost, additively manufactured, MEMS multiplexed electrospray sources; issues such as the lifetime of the devices, although very important for using the technology in a nanosatellite, were not addressed. However, preliminary experimental results suggest that the 3D-printed propulsion hardware reported in this study have a long lifespan. Electrospray devices using ionic liquid are typically operated with a square wave voltage to alternate positive and negative emission to avoid electrochemical effects (see for example [13]). However, the devices reported in this study were operated in DC, multiple times for several hours at a time, to collect the experimental data. This generated a thin crust (Fig. 9a); however, the crust is easily removed by simply flushing DI water using a common lab squeeze bottle (Fig. 9b), with no sonication, scrubbing, or high-speed/high-pressure water jets. The devices were cleaned and reused multiple times, showing no degradation in performance, suggesting that the emitters were not affected by the crust generation and removal. Moreover, SS 316L is a corrosion resistant stainless steel that, without the ZnONW forest, would not be able to transport the ionic liquid to the tips, which would prevent electrospray emission (Fig. 9c and d), further suggesting that the devices don't degrade during use, or due to forming and cleaning of the electrochemical crust. These promising results need to be investigated further.

5. Conclusions

This study reports the first proof-of-concept demonstration of low-cost, additively manufactured, bipolar MEMS multiplexed electrospray sources with ZnONW nanofluidics that produce pure ions from ionic liquids. These devices are comprised of an emitting electrode with a monolithic array of emitters and an extractor electrode that triggers electrohydrodynamic emission of ions from the emitter tips. The emitters are solid cones coated with a hydrothermally grown ZnONW forest that transports ionic liquid to the emitter tips. The extractor electrodes are 3D-printed using SS 316L via binder jetting. The emitting electrodes have up to 85 conical emitters (2.7×10^1 emitters/cm^2) and are 3D-printed using either SS 316L via binder jetting or FunToDo Industrial Blend resin via vat polymerization. The experimental characterization, in both polarities and in vacuum, of both kinds of devices, using an external collector electrode and EMI-BF_4 as propellant, shows pure-ion

emission with maximum per-emitter current of the order of microamperes, maximum per-emitter thrust of the level of a fraction of a micronewton, and ~95% beam transmission, resulting in 100% polydispersive efficiency and higher specific impulse than that of state-of-the-art devices. With advances in 3D printing hardware, these devices could reach emitter densities comparable to those realized in semiconductor cleanrooms or by using precision subtractive manufacturing methods, while incurring in significantly lower manufacturing costs and fabrication times. This will help democratize nanosatellite space hardware.

Funding sources

This work was sponsored by the Monterrey Tec-Massachusetts Institute of Technology (MIT) Nanotechnology program and the NewSat project. The NewSat project is co-funded by the Operational Program for Competitiveness and Internationalisation (COMPETE2020), Portugal 2020, the European Regional Development Fund (ERDF), and the Portuguese Foundation for Science and Technology (FTC) under the MIT Portugal program.

CRediT authorship contribution statement

Dulce Viridiana Melo Máximo: Methodology, Software, Validation, Formal Analysis, Investigation, Writing - original draft, Writing - review & editing, Visualization. **Luis Fernando Velásquez-García:** Conceptualization, Methodology, Resources, Writing - original draft, Writing - review & editing, Visualization, Supervision, Project Administration, Funding Acquisition.

Declaration of Competing Interest

The authors declare that they have no known competing financial interests or personal relationships that could have appeared to influence the work reported in this paper.

Acknowledgments

The authors would like to thank Asiga (Alexandria, Australia) for providing the DLP 3D printer used to create the polymeric devices, Tyler Teague from JETT Research & Proto Products (Fairview, TN, USA) for useful discussions on vat polymerization additive manufacturing and his help in tuning the recipe of the Asiga MAX X27 UV to print finely featured objects made of FTD-IB, and Yosef Kornbluth (Massachusetts Institute of Technology, Cambridge, MA, USA) for proofreading this scientific article.

Appendix A. Supporting information

Supplementary data associated with this article can be found in the online version at doi:10.1016/j.addma.2020.101719.

References

[1] G.P. Sutton, O. Biblarz, Rocket Propulsion Elements, ninth ed., John Wiley & Sons, Canada, 2016.
[2] J. Perel, J.F. Mahoney, R.D. Moore, A.Y. Yahiku, Research and development of a charged-particle bipolar thruster, AIAA J. 7 (3) (1969) 507–511, https://doi.org/10.2514/3.5137.
[3] A. Camps, Nanosatellites and applications to commercial and scientific missions (IntechOpen), Satell. Innov. Technol. (2019), https://doi.org/10.5772/intechopen.90039.
[4] R. Atem de Carvalho, J. Estela, M. Langer (Eds.), Nanosatellites: Space and Ground Technologies, Operations and Economics, John Wiley & Sons, Hoboken, NJ, USA, 2020.
[5] K. Holste, P. Dietz, S. Scharmann, K. Keil, T. Henning, D. Zschätzsch, M. Reitemeyer, B. Nauschütt, F. Kiefer, F. Kunze, J. Zorn, C. Heiliger, N. Joshi, U. Probst, R. Thüringer, C. Volkmar, D. Packan, S. Peterschmitt, K.-T. Brinkmann, H.-G. Zaunick, M.H. Thoma, M. Kretschmer, H.J. Leiter, S. Schippers, K. Hannemann, P.J. Klar, Ion thrusters for electric propulsion: scientific issues developing a niche technology into a game changer, Rev. Sci. Instrum. 91 (6) (2020), 061101, https://doi.org/10.1063/5.0010134.
[6] D. Krejci, P. Lozano, Space propulsion technology for small spacecraft, Proc. IEEE 106 (3) (2018) 362–378, https://doi.org/10.1109/JPROC.2017.2778747.
[7] I. Levchenko, K. Bazaka, Y. Ding, Y. Raitses, S. Mazouffre, T. Henning, P.J. Klar, S. Shinohara, J. Schein, L. Garrigues, M. Kim, D. Lev, F. Taccogna, R.W. Boswell, C. Charles, H. Koizumi, Y. Shen, C. Scharlemann, M. Keidar, S. Xu, Space micropropulsion systems for Cubesats and small satellites: from proximate targets to furthermost frontiers, Appl. Phys. Rev. 5 (1) (2018), 011104, https://doi.org/10.1063/1.5007734.
[8] A.A. Fomani, A.I. Akinwande, L.F. Velásquez-García, Resilient, nanostructured, high-current, and low-voltage neutralizers for electric propulsion of small spacecraft in low Earth orbit, J. Phys. Conf. Ser. 476 (2013), 012014, https://doi.org/10.1088/1742-6596/476/1/012014.
[9] I. Romero-Sanz, R. Bocanegra, J. Fernandez de la Mora, M. Gamero-Castaño, Source of heavy molecular ions based on Taylor cones of ionic liquids operating in the pure ion evaporation regime, J. Appl. Phys. 94 (5) (2003) 3599–3605, https://doi.org/10.1063/1.1598281.
[10] A. Borner, Z. Li, D.A. Levin, Prediction of fundamental properties of ionic liquid electrospray thrusters using molecular dynamics, J. Phys. Chem. B 117 (22) (2013) 6768–6781, https://doi.org/10.1021/jp402092e.
[11] L.F. Velásquez-García, A.I. Akinwande, M. Martinez-Sanchez, A planar array of micro-fabricated electrospray emitters for thruster applications, J. Microelectromech. Syst. 15 (5) (2006) 1272–1280, https://doi.org/10.1109/JMEMS.2006.879710.
[12] B. Gassend, L.F. Velásquez-García, A.I. Akinwande, M. Martinez-Sanchez, A microfabricated planar electrospray array ionic liquid ion source with integrated extractor, J. Microelectromech. Syst. 18 (3) (2009) 679–694, https://doi.org/10.1109/JMEMS.2009.2015475.
[13] R. Krpoun, H.R. Shea, Integrated out-of-plane nanoelectrospray thruster arrays for spacecraft propulsion, J. Micromech. Microeng. 19 (4) (2009), 045019, https://doi.org/10.1088/0960-1317/19/4/045019.
[14] D.G. Courtney, H.Q. Li, P. Lozano, Emission measurements from planar arrays of porous ionic liquid ion sources, J. Phys. D Appl. Phys. 45 (48) (2012), 485203.
[15] S. Dandavino, C. Ataman, C.E. Ryan, S.S. Chakraborty, D. Courtney, J.P.W. Stark, H.R. Shea, Microfabricated electrospray emitter arrays with integrated extractor and accelerator electrodes for the propulsion of small spacecraft, J. Micromech. Microeng. 24 (13) (2014), 075011, https://doi.org/10.1088/0960-1317/24/7/075011.
[16] F.A. Hill, E.V. Heubel, P. Ponce de Leon, L.F. Velásquez-García, High-throughput ionic liquid ion sources using arrays of microfabricated electrospray emitters with integrated extractor grid and carbon nanotube flow control structures, J. Microelectromech. Syst. 23 (5) (2014) 1237–1248, https://doi.org/10.1109/JMEMS.2014.2320509.
[17] K. Nakagawa, T. Tsuchiya, Y. Takao, Microfabricated emitter array for an ionic liquid electrospray thruster, Jpn. J. Appl. Phys. 56 (6S1) (2017), 06GN18, https://doi.org/10.7567/JJAP.56.06GN18.
[18] C. Guerra-Garcia, D. Krejci, P. Lozano, Spatial uniformity of the current emitted by an array of passively fed electrospray porous emitters, J. Phys. D Appl. Phys. 49 (12) (2016), 115503, https://doi.org/10.1088/0022-3727/49/11/115503.
[19] C. Chen, M. Chen, H. Zhou, Characterization of an ionic liquid electrospray thruster with a porous ceramic emitter, Plasma Sci. Technol. 22 (9) (2020), 094009, https://doi.org/10.1088/2058-6272/ab9528.
[20] M. Srivastava, S. Rathee, S. Maheshwari, T.K. Kundra, Additive Manufacturing: Fundamentals and Advancements, CRC Press, Boca Raton, 2019.
[21] A.K. Au, W. Huynh, L.F. Horowitz, A. Folch, 3D-printed microfluidics, Angew. Chem. Int. 55 (12) (2016) 3862–3881, https://doi.org/10.1002/anie.201504382.
[22] F. Li, N.P. Macdonald, R.M. Guijt, M.C. Breadmore, Increasing the functionalities of 3D printed microchemical devices by single material, multi material, and print-pause-print 3D printing, Lab on a Chip 19 (1) (2019) 35–49, https://doi.org/10.1039/c8lc00826d.
[23] A.P. Taylor, J. Izquierdo Reyes, L.F. Velásquez-García, Compact, magnetically actuated, additively manufactured pumps for liquids and gases, J. Phys. D Appl. Phys. 53 (35) (2020), 355002, https://doi.org/10.1088/1361-6463/ab8de8.
[24] A.P. Taylor, L.F. Velásquez-García, Miniaturized diaphragm vacuum pump by multi-material additive manufacturing, J. Microelectromech. Syst. 26 (6) (2017) 1316–1326, https://doi.org/10.1109/JMEMS.2017.2743020.
[25] L.F. Velásquez-García, SLA 3D-printed arrays of miniaturized, internally-fed, polymer electrospray emitters, J. Microelectromech. Syst. 24 (6) (2015) 2117–2127, https://doi.org/10.1109/JMEMS.2015.2475696.
[26] D. Olvera-Trejo, L.F. Velásquez-García, Additively manufactured MEMS multiplexed coaxial electrospray sources for high-throughput, uniform generation of core-shell microparticles, Lab on a Chip 16 (21) (2016) 4121–4132, https://doi.org/10.1039/C6LC00729E.
[27] Y. Xu, Nanofluidics: a new arena for materials science, Adv. Mater. 30 (2018), 1702419, https://doi.org/10.1002/adma.201702419.
[28] D. Thomas, S. Gilbert, Costs and cost effectiveness of additive manufacturing – a literature review and discussion, NIST Spec. Publ. 1176 (2014) 1–77, https://doi.org/10.6028/NIST.SP.1176.
[29] K. Law, Definitions for hydrophilicity, hydrophobicity, and superhydrophobicity: getting the basics right, J. Phys. Chem. Lett. 5 (4) (2014) 686–688, https://doi.org/10.1021/jz402762h.
[30] D.V. Melo-Máximo, L.F. Velásquez-García, Fully additively manufactured, nanostructured, miniature ionic liquid electrospray sources, in: IEEE 33rd International Conference on Micro Electro Mechanical Systems (MEMS),

Vancouver, BC, Canada, 2020. https://doi.org/10.1109/MEMS46641.2020.9056405.
[31] Z. Sun, G. Vladimirov, E. Nikolaev, L.F. Velásquez-García, Exploration of metal 3-D printing technologies for the microfabrication of freeform, finely featured, mesoscaled structures, J. Microelectromech. Syst. 27 (6) (2018) 1171–1185, https://doi.org/10.1109/JMEMS.2018.2875158.
[32] Z. Sun, L.F. Velásquez-García, Miniature, metal 3D-printed, multiplexed electrohydrodynamic gas pumps, Plasma Res. Express 2 (2) (2020), 025009, https://doi.org/10.1088/2516-1067/ab8f04.
[33] C. Yang, L.F. Velásquez-García, Low-cost, additively manufactured electron impact gas ionizer with carbon nanotube field emission cathode for compact mass spectrometry, J. Phys. D Appl. Phys. 52 (7) (2019), 075301, https://doi.org/10.1088/1361-6463/aaf198.
[34] G.F. Vander Voort, ASM Handbook, Volume 9: Metallography and Microstructures, ASM International, 2004, p. 681, https://doi.org/10.31399/asm.hb.v09.9781627081771.
[35] G. Yang, B. Wang, K. Tawfiq, H. Wei, S. Zhou, G. Chen, Electropolishing of surfaces: theory and applications, Surf. Eng. 33 (2) (2017) 149–166, https://doi.org/10.1080/02670844.2016.1198452.
[36] L.E. Greene, M. Law, J. Goldberger, F. Kim, J.C. Johnson, Y. Zhang, R.J. Saykally, P. Yang, Low temperature wafer-scale production of ZnO nanowire arrays, Angew. Chem. Int. 42 (26) (2003) 3031–3034, https://doi.org/10.1002/anie.200351461.
[37] S.P. Thompson, P.D. Prewett, The dynamics of liquid metal ion sources, J. Phys. D Appl. Phys. 17 (11) (1984) 2305–2321, https://doi.org/10.1088/0022-3727/17/11/018.
[38] P.C. Lozano, M. Martinez-Sanchez, Efficiency estimation of EMI-BF4 ionic liquid electrospray thrusters, in: 41st AIAA/ASME/SAE/ASEE Joint Propulsion Conference & Exhibit, Tucson, Arizona, 2005. https://doi-org/10.2514/6.2005–4388.
[39] M.A. Borysiewicz, ZnO as a functional material, a review, Crystals 9 (10) (2019) 505, https://doi.org/10.3390/cryst9100505.
[40] K.J. Terhune, L.B. King, Ion and droplet mass measurements of an electrospray emitter using E×B filter, in: Proc. 32nd Int. Electr. Propuls. Conf., Wiesbaden, Germany, 2011, IEPC-2011-29.
[41] B.L.P. Gassend (Ph.D. Thesis), Massachusetts Institute of Technology, Cambridge, MA, USA, 2007.
[42] C. Ryan, J.P.W. Stark, C. Ataman, S. Dandavino, S. Chakraborty, H. Shea, MicroThrust MEMS electrospray emitters – integrated microfabrication and test results, in: Presented at AAAF-ESA-CNES Space Propulsion, Bordeaux, France, 2012.
[43] B. Gassend, L.F. Velásquez-García, A.I. Akinwande, M. Martinez-Sanchez, A fully integrated microfabricated externally wetted electrospray thruster, in: 43rd AIAA/ASME/SAE/ASEE Joint propulsion Conference and Exhibit, Cincinnati, OH, USA, 2007, AIAA-2007-5182. https://doi.org/10.2514/6.2007-5182.
[44] E. Grustan-Gutierrez, M. Gamero-Castaño, Microfabricated electrospray thruster array with high hydraulic resistance channels, J. Propuls. Power 33 (4) (2017) 984–991, https://doi.org/10.2514/1.B36268.
[45] DLP 0.66 4K UHD DMD datasheet. https://www.ti.com/product/DLP660TE.
[46] B. Gassend, L.F. Velásquez-García, A.I. Akinwande, Precision in-plane hand assembly of bulk-microfabricated components for high voltage MEMS arrays applications, J. Microelectromech. Syst. 18 (2) (2009) 332–346, https://doi.org/10.1109/JMEMS.2008.2011115.
[47] L.F. Velásquez-García, A.I. Akinwande, M. Martínez-Sánchez, Precision hand assembly of MEMS subsystems using DRIE-patterned deflection spring structures: an example of an out-of-plane substrate assembly, J. Microelectromech. Syst. 16 (3) (2007) 598–612, https://doi.org/10.1109/JMEMS.2007.892931.